On the Study of Reconfigurable Intelligent Surfaces in the Near-Field Region

Peng Mei, *Member, IEEE*, Yang Cai, Kun Zhao, Zhinong Ying, *Fellow, IEEE*, Gert Frølund Pedersen, *Member, IEEE*, Xian Qi Lin, *Senior Member, IEEE*, and Shuai Zhang, *Senior Member, IEEE*

***Abstract*— As reconfigurable intelligent surface (RIS) is expected to be implemented with a large aperture in terms of wavelengths, using a RIS to perform near-field rather than conventional far-field communications might gain some benefits. The electric fields in the near-field region from the near-field focusing and conventional far-field RISs are simulated and compared to assess and validate the benefits. Two metrics of benefit distance and near-field gain are defined to characterize the electric fields in the near-field region. The cumulative distribution function (CDF) related to the near-field gain is calculated to describe the benefits in the area of interest where the total scan patterns from the near-field focusing and conventional far-field RISs are plotted. For demonstration, the benefit distance, near-field gain, and CDFs are presented and calculated for near-field focusing RISs with assigned focal distances of 80 and 300 mm. It is concluded that the benefit distance is a critical factor affecting the CDF directly. The effects of the size of a RIS and phase quantization of elements on the benefit distance, near-field gain, and CDF are also discussed. Moreover, the maximum focal distance of a near-field focusing RIS with a certain size is derived and specified. Finally, the electric fields of three prototypes (e.g., conventional far-field RIS, near-field focusing RISs with assigned focal distances of 500 and 1500 mm) at 26 GHz are measured and compared, where the benefit distances and near-field gains are experimentally observed.**

***Index Terms*— Cumulative distribution function (CDF), electric fields, near-field focusing, reconfigurable intelligent surfaces (RISs).**

I. Introduction

RECONFIGURABLE intelligent surfaces (RISs) are emerging communication paradigms, drawing lots of attention as they are promising solutions for the evolved 5G and upcoming 6G wireless communications [1]–[4]. RISs are kinds of surfaces that are composed of lots of artificial elements, where the reflection phase on each element can be controlled by switching electronic components, e.g., PIN diodes or RF switches [5]–[9]. As a result, RISs can direct the propagation of wireless signals, and suppress interference at desired receivers significantly, as well as enhance security with respect to non-intended receivers, by manipulating the radiation beams of the RIS intelligently.

Recently, investigations and discussions of RISs on the reliabilities, possibilities, and advantages have been widely done [10]–[17], which have theoretically and experimentally verified that RISs can greatly improve the spectral efficiency and channel capacity. In [15], comprehensive discussions on the differences, similarities, and performance comparisons between the RIS and relay node were carried out, concluding that the sufficiently large RISs can outperform relay-aided systems in terms of data rate while reducing the energy consumption and implementation complexity.

So far, most of the research work related to the RISs is mainly focused on studies, implications, and characterizations on practical RIS implementations following the far-field assumptions for far-field application scenarios. As a RIS is expected to be implemented with a large aperture in terms of wavelengths in the frequency range of interest, users or receivers might be distributed in the near-field region of a RIS (in some indoor application scenarios for example) as mentioned in [12]. In this case, the near-field assumptions should be adopted to analyze the performance of a RIS. There is, however, very little literature to systematically evaluate the electric-field activities in the near-field region of a RIS. Very recently, the near-field behaviors of RISs were studied in [18] with a simplified RIS model, where the mutual couplings among elements were not considered and the radiation pattern of each element was modeled as isotropic. Nevertheless, some potential benefits could be observed and predicted by using a RIS to perform near-field instead of the conventional far-field communications in a wireless system. In near-field wireless communications, the near-field focusing is usually capable of achieving focal spots with high energy in the near-field region serves as one of the critical technologies. The properties of the focal spot of a near-field focusing surface can be controlled freely by manipulating the phases of radiating elements.

In this article, it is the first time, to the authors' best knowledge, to carry out a thorough study and comparison of the characteristics of a RIS in its near-field region. The electric field is selected as the evaluation target, where the electric fields in the near-field region from the near-field focusing and conventional far-field RISs are simulated and compared. A metric of benefit distance is defined to quantify the spatial distance that the near-field focusing RIS can outperform the conventional far-field RIS in terms of electric-field amplitudes.

Manuscript received 27 August 2021; revised 9 December 2021; accepted 17 January 2022. Date of publication 4 February 2022; date of current version 9 November 2022. This work was supported in part by the RANGE Project and in part by the MARS2 Project. *(Corresponding author: Shuai Zhang.)*

Peng Mei, Yang Cai, Kun Zhao, Zhinong Ying, Gert Frølund Pedersen, and Shuai Zhang are with the Antennas, Propagation and Millimeter-Wave Systems (APMS) Section, Department of Electronic Systems, Aalborg University, 9220 Aalborg, Denmark (e-mail: sz@es.aau.dk).

Xian Qi Lin are with the School of Electronic Science and Engineering, University of Electronic Science and Technology of China, Chengdu 611731, China.

Color versions of one or more figures in this article are available at https://doi.org/10.1109/TAP.2022.3147533.

Digital Object Identifier 10.1109/TAP.2022.3147533

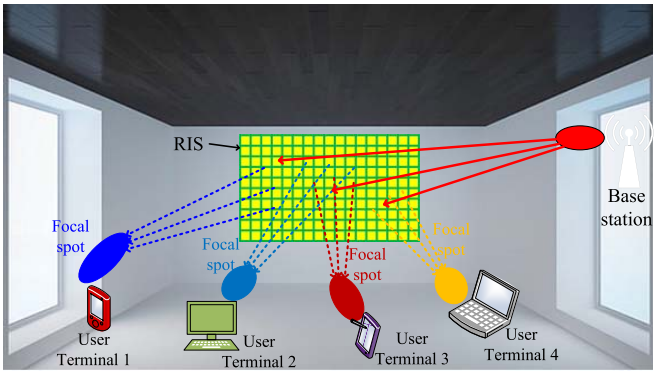

Fig. 1. Diagram of an application scenario of a near-field focusing RIS.

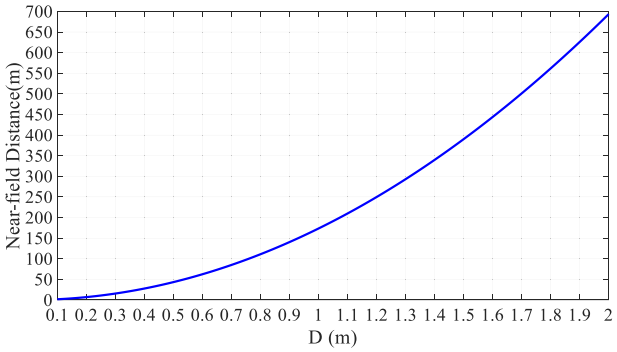

Fig. 2. Calculated near-field distance with different aperture sizes at 26 GHz using (1). (D is the diagonal length of the square-shaped aperture.)

Another metric of near-field gain is defined as the difference of the electric-field amplitudes from the near-field focusing and conventional far-field RISs at the same positions. Besides, the phase quantization of elements building a RIS and the size of a RIS are also studied to check their impacts on benefit distance and near-field gain. Further, the maximum actual focal distance of a certain-size RIS is also investigated. These studies offer profound and instructive guidelines for the designs of the near-field focusing RISs in practical applications. Three prototypes with distinct focusing properties have been fabricated; the electric fields along the boresight direction are measured to demonstrate the benefit distances and near-field gains.

The remainder of the article is organized as follows. Section II states the near-field application scenario of a RIS. The performance of a RIS in its near-field region is characterized in Section III, some metrics are defined to assess the benefits gained from a near-field focusing RIS. Also, the phase quantization of elements and the size of a RIS are studied in this section to examine their effects on the performance of a near-field focusing RIS. Three prototypes have been fabricated and measured in Section IV. Some conclusions are finally drawn in Section V.

II. Application Scenario Statement

To illustrate the potential use case when user terminals (e.g., mobile phone, laptop, iPad, etc.) are located at the near-field region of a RIS, an application scenario is shown in Fig. 1. The RIS will receive the electromagnetic waves first from the base stations and then direct them to user terminals by manipulating the reflection phase of the RIS intelligently. The electromagnetic characteristics emanating from an antenna, as is known to all, vary as a function of distance. As a result, the free space with respect to the antenna can be broadly divided into two regions, e.g., the near-field and far-field regions.

For an antenna, its near-field region is evaluated by the following equation [19]

$$d = \frac{2D^2}{\lambda} \tag{1}$$

where D is the minimal diameter of a sphere that encloses the antenna, for an aperture antenna, D is the diagonal length of the aperture antenna with a rectangular/square shape, and λ is the wavelength at the frequency of interest. Fig. 2 plots the near-field distance of a square-shaped RIS with different sizes at 26 GHz using (1). It is observed, for example, that the near-field distance of a RIS with a size of 500 mm $\times$ 500 mm is around 86.6 m. The near-field distance will be huge (several hundred meters) when the size of a RIS reaches the order of a few square meters, which can generally cover all space of an indoor scenario. As a result, it inspires one to consider using a RIS to perform near-field rather than conventional far-field communications in wireless systems. As the sizes of the receivers (e.g., user terminal) are much smaller than a RIS, the RIS is usually located at the far-field region of the receivers, indicating that the RIS will not affect the performance (e.g., radiation pattern, input impedance, etc.) of the receivers. On the other hand, the receivers do not disturb the field distributions in the near-field region due to the small sizes despite they are always located at the near-field region of the RIS.

III. Performance Analysis of a RIS in Its Near-Field Region

In this section, the performance of the near-field focusing RIS in the near-field region is studied and compared to that of the conventional far-field RIS to demonstrate the benefits that the near-field focusing RIS can gain. All the RISs presented in this section are the same type (dielectric-based RISs) and designed based on the same method. To follow and understand the work easily, this section has been divided into four subsections. In Section III-A, a 200 mm $\times$ 200 mm RIS is established with dielectric-based elements that are capable of continuous reflection phase shifts (e.g., 0–2π), and its electric fields are simulated and then compared with the conventional far-field RIS in the near-field region when the assigned focal spots located at different locations. Two metrics of benefit distance and near-field gain are defined and the cumulative distribution function (CDF) is calculated to assess the benefits that the near-field focusing RIS can gain. In Sections III-B and III-C, the effects of the phase quantization (e.g., 1- and 2-bit) of elements building the RIS and the size of the RIS on the benefit distance, near-field gain, and CDF have been examined. The maximum actual focal distance of a certain-size RIS is also studied in subsection *D*. The results obtained in Sections III-B, III-C, and III-D provide some general guidelines for the designs of the near-field focusing RISs in practical applications.

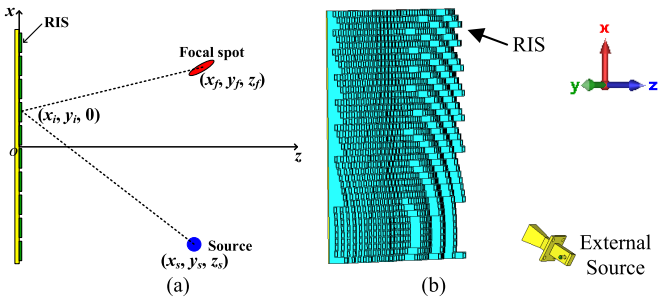

Fig. 3. (a) Simple diagram of a RIS illuminated with an external source to achieve a focal spot in the near-field region. (b) An Example of the simulation model in CST software.

A. Simulation Setup and Basic Metric Definitions

For a conventional far-field RIS, the radiation beam of the RIS is typically characterized by a solid angle (θ, φ) in the spherical coordinate. By contrast, the location of the focal spot of a near-field focusing RIS is positioned with $(r, \theta,$ and $\varphi)$ in the spherical coordinate, indicating that we have one more degree of freedom to control the focal spot.

Still, the manipulations of the focal spot of a near-field focusing RIS rely on controlling the reflection phase of each element of the RIS. Fig. 3(a) presents a simple diagram of a RIS illuminated with an external source, where the external source can offer either a spherical or plane wave. The RIS is usually composed of periodic elements with a periodicity of around half-wavelength at the frequency of interest in free space. The RIS first receives the electromagnetic waves from the external source and then can achieve a focal spot in the near-field region. For a focal spot at a specific position of (x_f, y_f, z_f), the phase on element i of the RIS is formulated as

$$\varphi(x_i, y_i, 0) = -\frac{2\pi}{\lambda}\left(\sqrt{(x_s - x_i)^2 + (y_s - y_i)^2 + (z_s)^2} + \sqrt{(x_f - x_i)^2 + (y_f - y_i)^2 + (z_f)^2}\right) \quad (2)$$

where (x_s, y_s, z_s) is the location of the phase center of the external source, $(x_i, y_i, 0)$ is the location of the element i in the RIS, and λ is the wavelength at the frequency of interest.

To demonstrate the performance and properties of a near-field focusing RIS, we build a 200 mm $\times$ 200 mm RIS by using dielectric-based reflective elements with a periodicity of 5 mm for the sake of saving simulation time. The detailed information about the dimensions and frequency responses of the dielectric-based elements can be found in the Appendix. The reflection phase of the element can be controlled by tuning the height of the element. The RIS is obliquely illuminated with a linearly-polarized horn antenna that generates spherical waves, where the horn antenna can offer a gain of 10 dBi at 26 GHz. According to the radiation patterns of the horn antenna at 26 GHz, the location of the phase center of the horn antenna is set as (95 mm, 0, 106.5 mm) to eliminate its blockage effects and offer a good aperture illumination. The illumination taper can also be found in the Appendix. Using (2), we can calculate the phase distributions of elements on the RIS at 26 GHz with assigned focal distances of

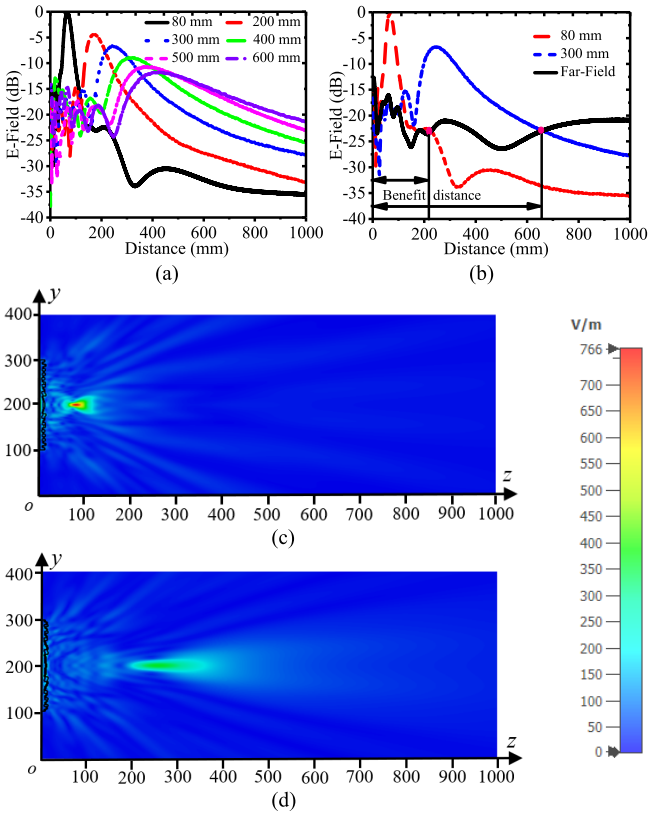

Fig. 4. Near-field focusing performance of a RIS. (a) The electric field along the boresight direction with the assigned focal distances of 80, 200, 300, 400, 500, and 600 mm. (b) The electric field along the boresight direction with the assigned focal distance of 80 and 300 mm, and the referred far-field. (c) The electric-field distribution on the *yoz* plane with the assigned focal distance of 80 mm. (d) The electric-field distribution on the *yoz* plane with the assigned focal distance of 300 mm. [The units for *y*- and *z*-axis are millimeters in both Fig. 4(c) and (d).]

80, 200, 300, 400, 500, and 600 mm along the boresight direction (*z*-direction). The near-field focusing performance of the RISs is simulated with CST Microwave Studio software. An example of a simulation model established in CST is depicted in Fig. 3(b). Fig. 4(a) presents the electric fields in the *z*-direction from 0 to 1000 mm (corresponding to 0–87λ, λ is the wavelength at 26 GHz). It is observed that the simulated actual focal distance (the location that the peak electric-field amplitude locates) is smaller than the assigned focal distance. The focal distance discrepancy between the locations of the actual and assigned focal spots is named focal shift, which is attributed to the field-spreading factor $1/R$ as explained in [20] and [21]. The focal shift becomes increasingly remarkable and the focal spot is less concentrated with the increment of the assigned focal distance as seen in Fig. 4(a). Indeed, the electric-field distributions on the *yoz* plane of the RISs with assigned focal distances of 80 and 300 mm are plotted and shown in Fig. 4(c) and (d), where it is observed that the shape of the focal spot becomes longer for a larger assigned focal distance.

To illustrate the benefits from a RIS performing the near-field focusing, the electric fields of the conventional far-field RIS (RIS acts as a conventional directive reflector) along the boresight direction are also simulated. As seen in Fig. 4(b), there is no focal spot for the conventional far-field RIS from

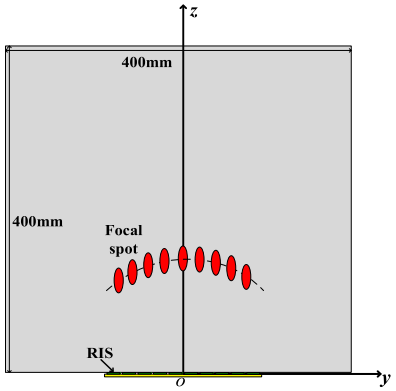

Fig. 5. Diagram of the scanning radiation beam/focal spot on the *yoz* plane.

0 to 1000 mm. The intersection points of the electric fields between the near-field focusing and conventional far-field RISs can be observed from Fig. 4(b), where the longitude distance of the intersection point is defined as benefit distance here. Within the benefit distance, the electric fields from the near-field focusing RIS are stronger than the counterparts from the conventional far-field RIS as seen in Fig. 4(b). It should be mentioned here that the electric field from the near-field focusing RIS will not intersect with that from the conventional far-field RIS again beyond the benefit distance. Besides, the benefit distance is becoming larger with the increment of the focal distance as observed in Fig. 4(b).

To assess the benefits, we can gain in the near-field region by using the near-field focusing RIS instead of the conventional far-field RIS. A CDF related to the electric-field enhancement is proposed and defined as

$$F(x) = P((E_{focusing} - E_{ref}) \leq x) \tag{3}$$

where $E_{focusing}$ is the electric-field amplitude from the near-field focusing RIS at a specific location and E_{ref} is the electric-field amplitude from the conventional far-field RIS at the same location. The difference between $E_{focusing}$ and E_{ref} in logarithmic scale is named near-field gain here (e.g., Near-field fain $= E_{focusing} - E_{ref}$), which also stands for the ratio $E_{focusing}/E_{ref}$ in the linear domain. When a near-field gain is positive, it means $E_{focusing}$ is stronger than E_{ref}. The CDF implies the probability of the near-field gain less than a certain value in the area of interest that could be a line, a plane, or a volume.

To effectively accommodate scenarios with mobile users, the RIS should also be able to steer its radiation beam or focal spot. By selecting the points with the highest powers from all scanning beams or focal spots within a 2-D or 3-D space, a total scan pattern can be formed in a plane or volume accordingly. For demonstration, we select an area of 400 mm $\times$ 400 mm on the *yoz* plane as the area of interest as shown in Fig. 5 to reduce the simulation time and eliminate the blockage effects of the external source (horn antenna). The total scan patterns from the near-field focusing and conventional far-field RISs are simulated and plotted, where the CDFs related to the near-field gain can be calculated then according to the total scan patterns.

Here, we investigate and calculate the CDFs related to the near-field gain of the near-field focusing RISs.

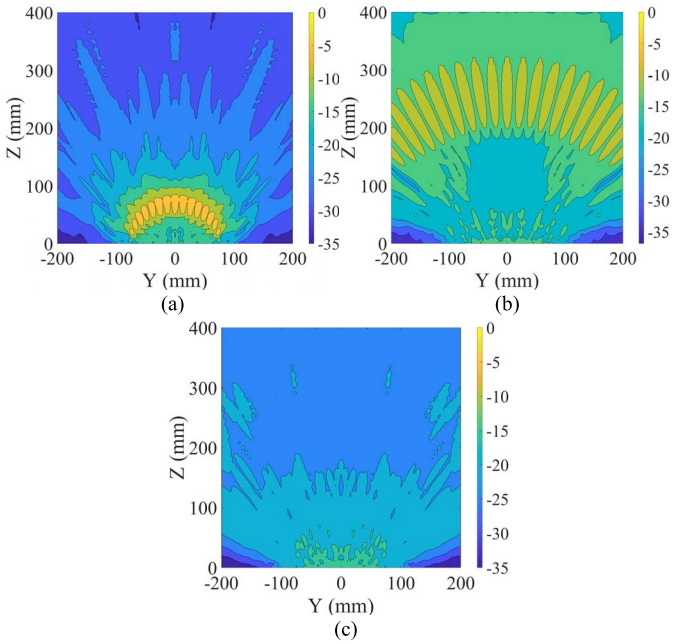

Fig. 6. Total scan patterns within the area of interest (400 mm $\times$ 400 mm on the *yoz* plane) at 26 GHz. (a) Near-field focusing RIS with an assigned focal distance of 80 mm. (b) Near-field focusing RIS with an assigned focal distance of 300 mm. (c) Conventional far-field focusing RIS. [All values are normalized to the maximum electric-field amplitude of Fig. 6(a).]

Fig. 6(a) and (b) plots the total scan patterns of the near-field focusing RIS with assigned focal distances of 80 and 300 mm in the area of interest, respectively. It is observed that the focal spots are scanned along the arcs that correspond to their respective focal distance. The total scan pattern of the conventional far-field RIS at the same area of interest is also plotted in Fig. 6(c). As a result, the corresponding CDFs of the near-field focusing RISs with assigned focal distances of 80 and 300 mm are calculated and shown in Fig. 7.

Some information can be obtained from the calculated CDFs shown in Fig. 7. Note that the results in Fig. 7 have already included the conventional far-field RIS case as the near-field gain is defined as the difference between $E_{focusing}$ and E_{ref}. The maximum near-field gains are 15 and 17 dB for the near-field focusing RISs with assigned focal distances of 80 and 300 mm, respectively. On the other hand, the probability that the electric fields from a near-field focusing RIS stronger than the counterparts from the conventional far-field RIS in the area of interest with respect to a certain near-field gain value can be directly observed from the CDFs shown in Fig. 7. For the near-field focusing RIS with an assigned focal distance of 80 mm, for example, the value of the corresponding CDF is 0.78 when the near-field gain is 0 dB. The value of 0.78 implies the region that electric fields from the near-field focusing RIS are stronger than the counterparts of the conventional far-field RIS accounts for 22% of the area of interest (400 mm $\times$ 400 mm). By contrast, the value of the CDF is only 0.09 when the near-field gain is 0 dB for the near-field focusing RIS with an assigned focal distance of 300 mm.

As seen in Fig. 7, the CDFs of the near-field focusing RISs with assigned focal distances of 80 and 300 mm are greatly distinct (the slopes of the curves are different). For example,

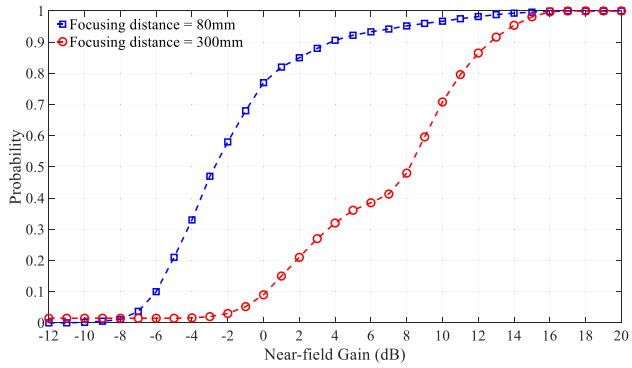

Fig. 7. Calculated CDFs of near-field gain of near-field focusing RISs with assigned focal distances of 80 and 300 mm.

the probabilities differ noticeably when the near-field gain is 0 dB, they are 0.78 and 0.09. The differences of the CDFs can be explained from the 1-D electric fields shown in Fig. 4(b). Compared to the dimension of the area of interest [400 mm × 400 mm (*yoz* plane)], the electric fields from the near-field focusing RIS with an assigned focal distance of 300 mm are always stronger than those of the conventional far-field RIS within 400 mm except for at some points close to the RIS as the benefit distance of the near-field focusing RIS is around 650 mm. By contrast, as the benefit distance with an assigned focal distance of 80 mm is only around 180 mm, the electric fields of the near-field focusing RIS are only stronger than those of the conventional far-field RIS within 180 mm. Beyond the benefit distance (from 180 to 400 mm), the electric fields of the near-field focusing RIS are weaker than those of the conventional far-field RIS. As a result, it can be concluded that the benefit distance is a critical factor affecting the CDF.

It should be mentioned here, the CDF is also affected by the size of the area of interest. Specifically speaking, for a near-field focusing RIS with an assigned focal distance of 300 mm, the CDFs will be different when the areas of interest are 400 mm × 400 mm and 600 mm × 600 mm. The maximum near-field gains might be the same but the probabilities that the near-field gain is higher than an identical value will be distinct.

B. Effects of Phase Quantization on Near-Field Focusing Performance

The element enabled by liquid crystal technologies can offer continuous phase shifts by controlling the applied electric fields [22]–[24]. It, however, suffers from high loss and complicated manufacturing processes. By contrast, the 1-bit reflection phase has been widely adopted to enable beam-steerable reflectarray antennas by loading PIN diodes on each element [5]–[8]. The impacts of phase quantization on radiation patterns of a reconfigurable reflectarray antenna have been investigated and reported in [25]. It was concluded that the phase quantization would reduce the gain and increase the sidelobe level of a reflectarray antenna. Here, the effects of the phase quantization (1-bit, 2-bit, and continuous reflection phases) on the near-field focusing performance of a RIS are investigated.

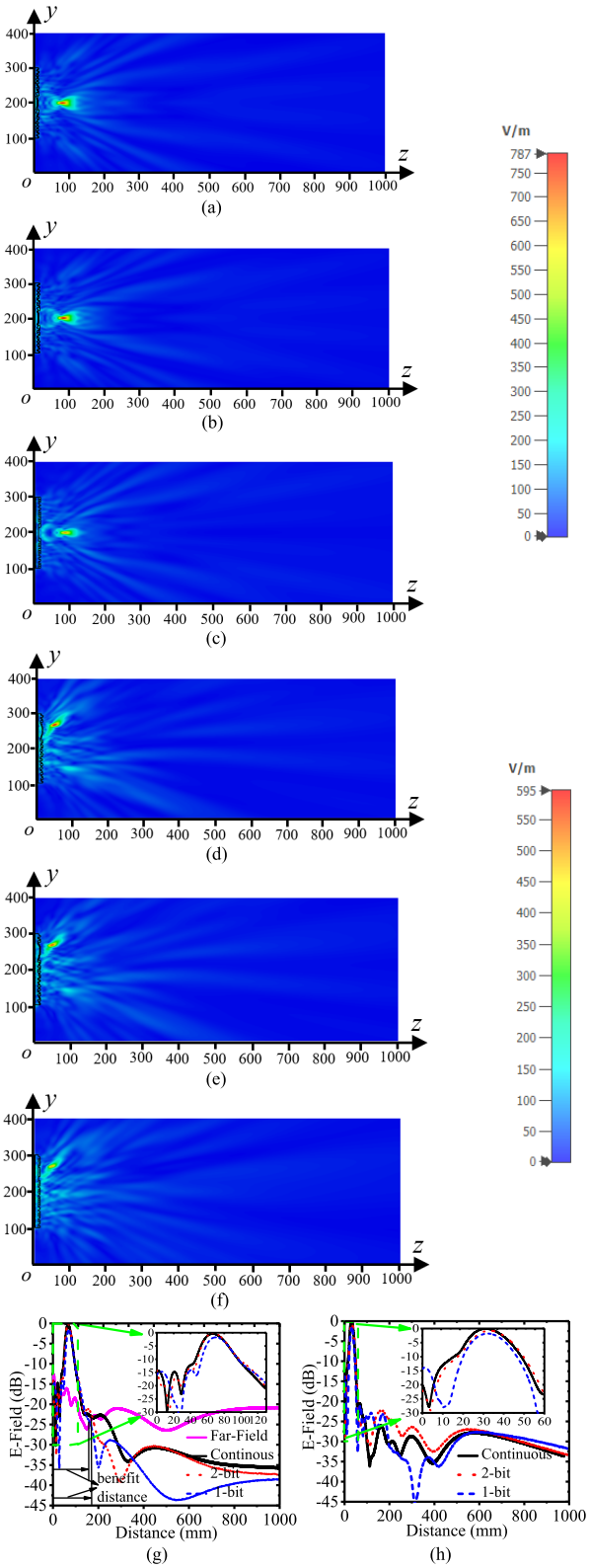

Fig. 8. Electric fields of a RIS with an assigned focal distance of 80 mm under different phase quantization. (a) Continuous with a focal spot at broadside direction. (b) 2-bit with a focal spot at broadside direction. (c) 1-bit with a focal spot at broadside direction. (d) Continuous with a focal spot at 60° off-broadside direction. (e) 2-bit with a focal spot at 60° off-broadside direction. (f) 1-bit with a focal spot at 60° off-broadside direction. (g) Electric fields at the boresight direction with $y = 0$ mm. (h) Electric fields at the boresight direction with $y = 68$ mm. [The units for y- and z-axis are millimeters in Fig. 8(a)–(f).]

For demonstration, a 200 mm × 200 mm RIS is selected. The electric fields of the RIS are simulated and checked at both broadside and 60° off-broadside directions when the assigned focal distances are 80 and 300 mm, respectively. For the focal spot at broadside direction, the 2-D electric fields on the *yoz* plane for the RISs with assigned focal distances of 80 and 300 mm are shown in Figs. 8(a)–(c) and 9(a)–(c), respectively, when the elements offer continuous, 2-bit, and 1-bit reflection phases. Figs. 8(g) and 9(g) compare the 1-D electric fields along the boresight direction at $y = 0$ mm, where the position and beamwidth of the focal spot can still be maintained with the three different phase quantization. However, the benefit distances and maximum electric-field amplitudes are shortened and reduced for the RIS with a 1-bit phase quantization, respectively. They are more remarkable when the focal distance is 300 mm as can be observed in Fig. 9(g). According to the 2-D electric fields on the *yoz* plane for the assigned focal distances of 80 and 300 mm are plotted in Figs. 8(d)–(f) and 9(d)–(f), and 1-D electric fields along the boresight direction at $y = 68$ and 212 mm that the maximum electric-field amplitudes go through these lines as shown in Figs. 8(h) and 9(h), the peak electric-field amplitudes, positions, and the beamwidths of the focal spots are all quite stable and close to each other under the three different phase quantization when the focal spots are 60° off-broadside direction.

As can be observed in Figs. 8 and 9, the sidelobe levels of the RISs with continuous and 2-bit phase quantization are very close to each other, while they become worse for the RIS with a 1-bit phase quantization. The effects of phase quantization on the near-field focusing RISs are in line with the results in [29] in terms of sidelobe levels.

The total scan patterns of the RIS composed of 1-bit elements are also simulated in the area of interest (400 mm × 400 mm) and plotted in Fig. 10 when the assigned focal distances are 80 and 300 mm, where the focal spots are still scanned along the arcs. According to the total scan patterns shown in Figs. 6(c) and 10, the CDFs related to the near-field gain of the near-field focusing RIS composed of 1-bit elements are calculated and plotted as shown in Fig. 11 when the assigned focal distances are 80 and 300 mm. The CDFs of the corresponding near-field focusing RISs composed of elements with continuous reflection phases are also plotted in Fig. 11 for comparison. As seen in Fig. 11(a), it is observed that the maximum near-field gains are very close to each other for the RIS with continuous and 1-bit phase quantization when the focal distance is 80 mm. As the benefit distance of the RIS composed of 1-bit elements is slightly smaller as seen in Fig. 8(g), the probability of the RIS composed of 1-bit elements is slightly higher than that of the RIS composed of the elements with continuous phases when the near-field gain is equal to 0 dB, where the probabilities are 0.81 and 0.78, respectively.

By contrast, when the assigned focal distance is 300 mm, the maximum near-field gains of the RISs composed of elements with continuous and 1-bit reflection phases are 17 and 15 dB, respectively, as observed in Fig. 11(b). As the benefit distance of the RIS composed of elements with 1-bit phase quantization

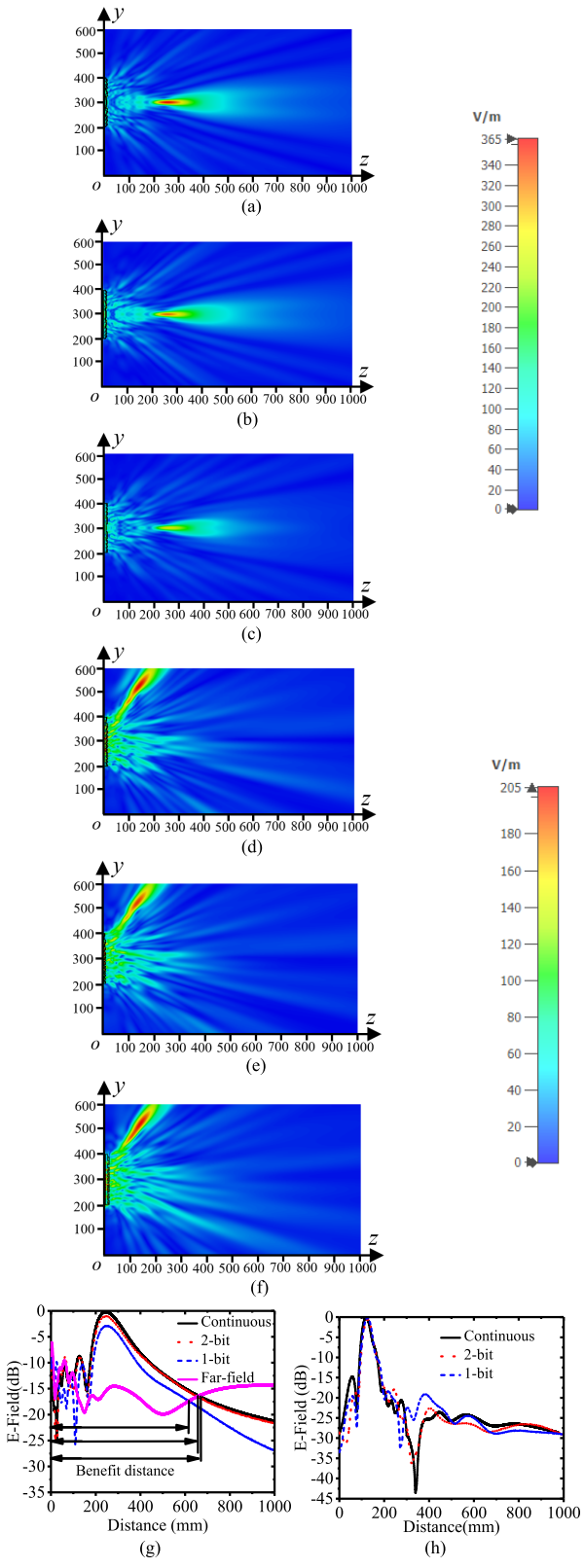

Fig. 9. Electric fields of a RIS with an assigned focal distance of 300 mm under different phase quantization. (a) Continuous with a focal spot at broadside direction. (b) 2-bit with a focal spot at broadside direction. (c) 1-bit with a focal spot at broadside direction. (d) Continuous with a focal spot at 60° off-broadside direction. (e) 2-bit with a focal spot at 60° off-broadside direction. (f) 1-bit with a focal spot at 60° off-broadside direction. (g) Electric fields at the boresight direction with $y = 0$ mm. (h) Electric fields at the boresight direction with $y = 212$ mm. [The units for y- and z-axis are millimeters in Fig. 9(a)–(f).]

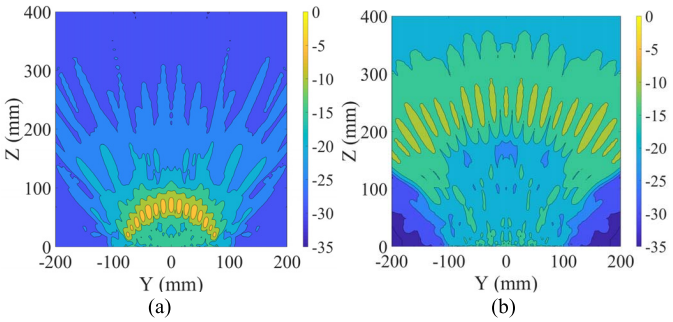

Fig. 10. Total scan patterns within an area of 400 mm × 400 mm on the *yoz* plane at 26 GHz. (a) 1-bit near-field focusing RIS with an assigned focal distance of 80 mm. (b) 1-bit near-field focusing RIS with an assigned focal distance of 300 mm. [All values are all normalized to the maximum electric-field amplitude of Fig. 6(a).]

is remarkably smaller as shown in Fig. 9(g), the probability of the RIS composed of 1-bit elements is noticeably higher than that of the RIS composed of the elements with continuous phases when the near-field gain is equal to 0 dB, where the probabilities are 0.21 and 0.09, respectively.

According to the results shown in Figs. 8, 9, and 11, the effects of the phase quantization on the performance of a near-field focusing RIS highly rely on the specific position of the focal spot (e.g., focal distance, broadside or off-broadside direction, etc.). In general, a 2-bit phase quantization can achieve comparable and similar results with the continuous reflection phase in terms of maximum electric-field amplitude, benefit distance, and sidelobe levels. By contrast, the maximum electric-field amplitude will be reduced for the RIS with a 1-bit phase quantization, resulting in lowering the maximum near-field gain. When the focal distance is large, the benefit distance will be noticeably shortened for the RIS with a 1-bit phase quantization, which leads to a higher probability in terms of the CDF in the area of interest when the near-field gain is equal to a certain value as demonstrated in Fig. 11.

C. Effects of the RIS's Size on Near-Field Focusing Performance

No doubt that the aperture size of a RIS is one of the most important parameters for RISs designs, as it does not only lead to different beamforming gains but also affects how much power (electromagnetic waves) that a RIS can capture from free space. To examine the effects of the size of a near-field focusing RIS on benefit distance, near-field gain, and CDF, the electric fields of the near-field focusing and conventional far-field RISs with dimensions of 200 mm × 200 mm and 300 mm × 300 mm are simulated and compared. For a fair comparison, the external sources (horn antennas) to illuminate the 200 mm × 200 mm and 300 mm × 300 mm RISs are identical, and the relative positions of the horn antennas with respect to the RISs should be kept the same as shown in Fig. 12 so that the RISs can capture the same power from the horn antennas. In other words, the electric-field illumination tapers on the RISs are the same for the two cases.

For demonstration, we simulate the electric fields along the boresight direction from the near-field focusing RIS with an assigned focal distance of 300 mm and the conventional

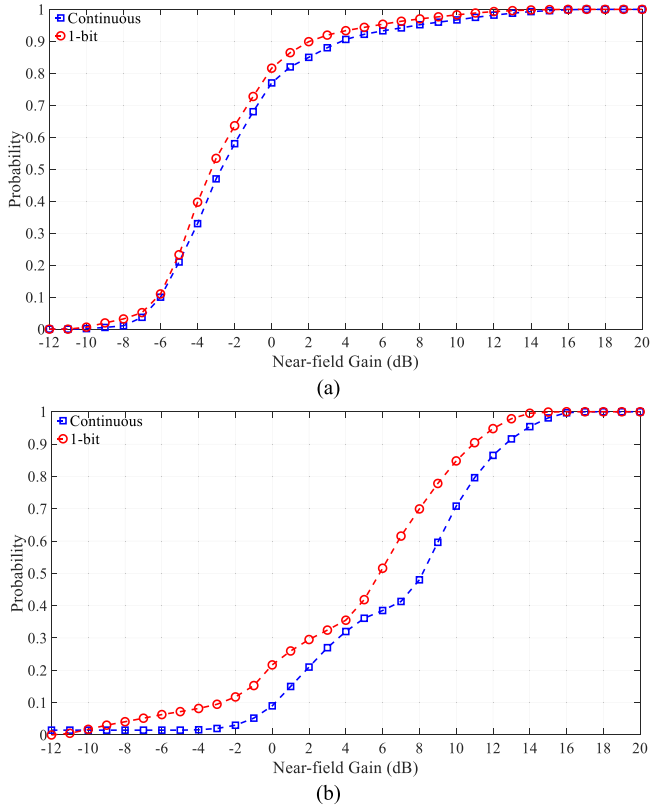

Fig. 11. Calculated CDFs. (a) Continuous and 1-bit near-field focusing RISs with an assigned focal distance of 80 mm. (b) Continuous and 1-bit near-field focusing RISs with an assigned focal distance of 300 mm.

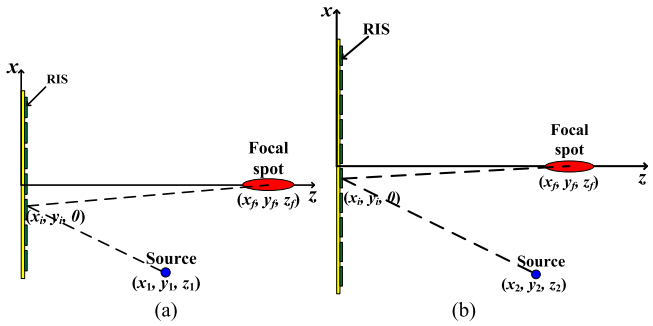

Fig. 12. Configurations of the RISs with different sizes. (a) 200 mm × 200 mm. (b) 300 mm × 300 mm.

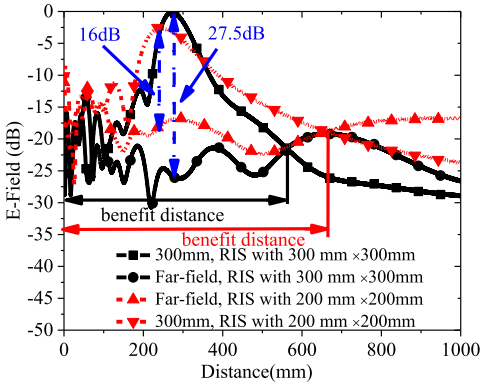

Fig. 13. Electric fields along the boresight direction for the RISs with dimensions of 200 mm × 200 mm and 300 mm × 300 mm.

far-field RIS as shown in Fig. 13, where the counterparts from the 200 mm × 200 mm RIS are also plotted for comparison.

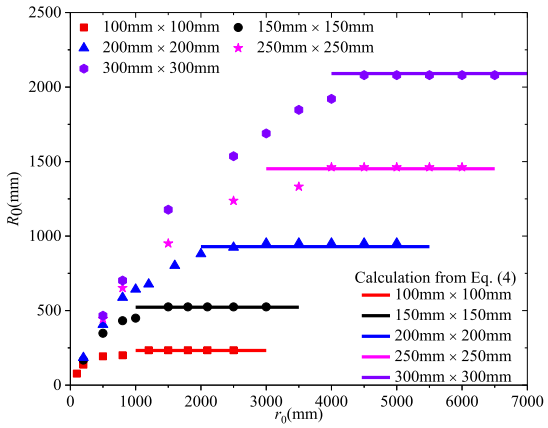

Fig. 14. Relationship between the assigned focal distance and the actual focal distance of different size RISs.

As seen in Fig. 13, the focal shift of a large-size RIS still exists but is weaker than that of a small-size RIS. A large-size RIS can offer a bigger maximum electric-field amplitude at the actual focal distance, where a 2.5 dB electric-field amplitude higher can be observed for the large-size RIS from Fig. 13. On the other hand, the large-size RIS receives the same power as the small-size RIS from the horn antennas, the received power will be uniformly distributed on the RIS after the conventional far-field RIS converting the spherical wave from the horn antenna to a plane wave. As a result, the electric fields along the boresight direction (electric-field density) from the large-size conventional far-field RIS are noticeably smaller than those of the small-size conventional far-field RIS as demonstrated in Fig. 13. The smaller electric field will lead to the near-field gain of the large-size RIS greater than that of the small-size RIS. The near-field gain at the actual focal distance is 27.5 dB for the large-size RIS, while it is 16.0 dB for the small-size RIS when the RISs have the same assigned focal distances of 300 mm.

As the maximum electric-field amplitude from the large-size RIS is higher than that of the small-size RIS, the corresponding beamwidth of the focal spot is narrower, leading to a smaller benefit distance as can be observed in Fig. 13. The smaller benefit distance will affect the CDF in the area of interest (e.g., 400 mm × 400 mm) accordingly following the results shown in Fig. 11, where the maximum near-field gain is higher and the probability is smaller with respect to a certain near-field gain in the same area of interest.

D. Maximum Focal Distance of a RIS With a Certain Size

Though the results so far suggest that performing near-field focusing can indeed enhance the field amplitude in the desired area greatly, the near-field gains of a given RIS size decay with an increased focusing distance as mentioned previously. According to the electric-field distributions under different assigned focal distances shown in Fig. 4(a), there should be a maximum actual focal distance for a certain-size RIS.

A general case is considered here to study the maximum actual focal distance of a RIS, where the RIS is implemented with half-wavelength elements and illuminated with a normal incidence plane wave. The corresponding actual focal distances are simulated for RISs with different sizes when

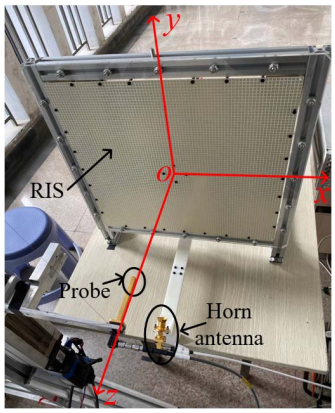

Fig. 15. Measurement setup.

the assigned focal distances vary as shown in Fig. 14, where R_0 and r_0 represent the actual and assigned focal distances, respectively. As seen in Fig. 14, all the actual focal distances converge to their respective maximum values for different size RISs when assigned focal distances reach beyond certain values. It is also found that the maximum values are much less than the calculated near-field regions of RISs with different sizes using (1). Besides, it is observed that, from Fig. 14, for a fixed assigned focal distance, the effect of the focal shift is noticeably weakened as the size of the RIS increases, which is consistent with the results shown in Fig. 13.

As can be seen in Fig. 14, the maximum actual focal distance is directly related to the size of the RIS, and it should also be associated with the frequency of interest. A proper formula should be formulated to characterize the relationship among the maximum actual focal distance, the size, and the operating frequency of a RIS. We know that the calculation of near-field region (2D^2/λ) involves the size of a RIS and the frequency of interest. Therefore, we are trying to normalize the maximum actual focal distance to 2D^2/λ. After doing some calculations, the ratios of the maximum actual focal distances of different size RISs to their respective 2D^2/λ are almost the same, which can be broadly formulated as follows:

$$\frac{R_{0\max}}{2D^2/\lambda} \approx 0.067 \tag{4}$$

where $R_{0\max}$ is the maximum actual focal distance of a RIS. The maximum actual distances of RISs with different sizes are calculated with (4) and also plotted in Fig. 14, where the results from (4) align well with the simulations.

Equation (4), on one hand, indicates that the maximum actual focal distance of a RIS is only 0.067 times of its near-field region calculated with 2D^2/λ. It, on the other hand, imposes a threshold on the maximum actual focal distance that a RIS can reach, which can be served as guidelines in practical designs of RISs.

IV. Experimental Measurement

From the above analyses, it is concluded that the benefit distance is a critical metric affecting the CDF directly. Besides, the results presented in Section III are obtained by studying the RISs implemented with dielectric-based reflective elements for the sake of saving simulation time. The RIS

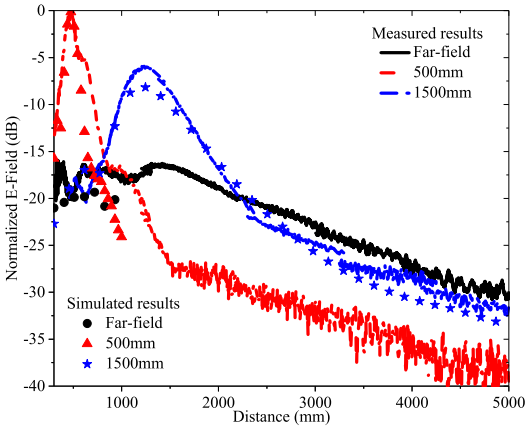

Fig. 16. Measured electric fields along the boresight direction from 300 to 5000 mm from the three prototypes. (Far-field, near-field focusing with assigned focal distances of 500 and 1500 mm.)

typically consists of thin PCB-based elements in practical RIS implementations [6]–[8]. Nevertheless, the conclusions derived in Section III are also applicable to the RISs composed of PCB-based elements. To this end, the experimental measurements are carried out on the PCB-based RISs. It will be a huge workload to measure the total scan patterns of the near-field and the conventional far-field RISs in the area of interest. As a result, 1-D electric fields are measured to demonstrate the benefit distance and near-field gain.

To reduce the measurement complexity and cost, we have fabricated three prototypes with each dimension of 400 mm × 400 mm (e.g., conventional far-field RIS, near-field focusing RISs with assigned focal distances of 500 and 1500 mm). The elements building the prototypes are single-layered and double square-loop structures [26]. The substrates used in the prototypes are all Rogers RO4350B with a thickness of 1.524 mm, a dielectric constant of 3.55, and a loss tangent of 0.004 [27]. The electric fields of the three prototypes along the boresight direction from 300 to 5000 mm have been measured and compared. The measurement setup is demonstrated in Fig. 15, where the origin of the coordinate is exactly located at the center of the prototype. The horn antenna serves as an external source to illuminate the RIS and the open-ended waveguide acts as a probe to detect the fields.

Fig. 16 plots the electric fields of the three prototypes along the boresight direction (z-direction, $x = 0$ mm, $y = 0$ mm) from 300 to 5000 mm (26λ–433.3λ, λ is the wavelength at 26 GHz). Some discontinuities can be observed on curves in Fig. 16 as the scanner in the measurement setup can only automatically scan 1000 mm each time, we have to move the measurement setup manually several times to finish the measurement from 300 to 5000 mm. Since the dimensions of the fabricated prototypes are 400 mm × 400 mm, our available computer is not competent in fully simulating such large models with CST. As a result, some discrete simulated results are provided in Fig. 16 for comparison with the measurements. As seen in Fig. 16, the measured focal distances agree well with the simulations, while the measured electric-field amplitudes at the actual focal distances are smaller than those of the simulated results. There are two possibilities to result in the discrepancies: One is that the probe does not align

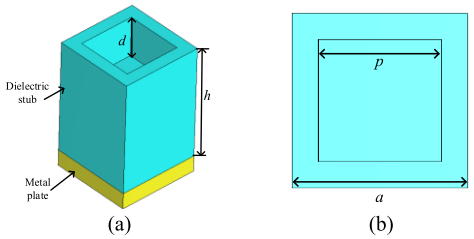

Fig. 17. Geometry of the dielectric-based element. (a) Perspective view. (b) Front view. ($a = 5$ mm, $p = 3.5$ mm, and $d = 2.5$ mm.)

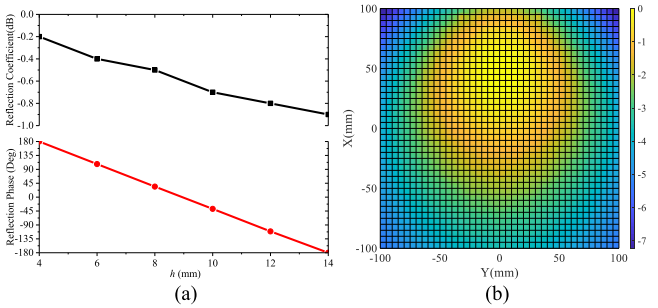

Fig. 18. (a) Reflection phase and coefficient of the dielectric-based element with different values of h. (b) Edge illumination of the simulation model shown in Fig. 4 at 26 GHz.

with the center of the prototype during the measurement; the other is the deviation of the focal spot that the focal spot is not exactly located at the boresight direction (z-direction, $x = 0$ mm, $y = 0$ mm) for the prototypes. The deviation of the focal spot is caused by the assembly error that the relative position of the horn antenna with respect to the prototype is not the same as the simulation. From the measured results in Fig. 16, the benefit distances and near-field gains can be observed, which are all consistent with the results described in Section III.

V. Conclusion

The near-field behaviors of a near-field focusing RIS are thoroughly studied in this article. By comparing the electric fields from the near-field focusing and conventional far-field RISs in the near-field region, it is found that the electric fields from the near-field focusing RIS are stronger than those from the conventional far-field RIS in some regions. To assess the benefits, we can gain by using near-field focusing RIS, two metrics of benefit distance and near-field gain are defined, and CDF related to the electric-field enhancement has been calculated.

By studying the near-field focusing RISs with assigned focal distances of 80 and 300 mm, it is concluded that a large focal distance contributes to a larger benefit distance and a smaller near-field gain, and the benefit distance affects the CDF directly. A large benefit distance usually results in a smaller probability in terms of CDF in the area of interest when the near-field gain is equal to a certain value. The effects of the phase quantization of elements building a RIS and the size of a RIS on benefit distance, near-field gain, and CDF are also studied. It is concluded that a 1-bit phase quantization shortens the benefit distance and reduces the maximum near-field gain. Besides, a large-size RIS leads to a smaller benefit distance and enhanced near-field gain. The major conclusions observed from extensive simulation campaigns are verified

through the electric fields along the boresight direction of the three prototypes, where the benefit distances and near-field gains are experimentally observed.

If the entire space of the room is within the near-field region of a RIS, using a RIS to perform near-field focusing indeed brings some benefits compared to the conventional far-field RIS in indoor wireless communication application scenarios. Moreover, we can assess the near-field gain according to the transmitted power from the base station to determine the size of the RIS accordingly if the deployment scenario and the desired power that users should receive are known.

APPENDIX

The dimensions of the dielectric-based element used in Section III are shown in Fig. 17. A cuboid air void is etched on the top of the dielectric stub to improve the relationship between the reflection phase and height of the dielectric stub (h). When the dimensions of a, p, and d are properly assigned, the dielectric-based elements can offer minor loss and linear reflection phase with a 2π reflection phase coverage under different values of h as shown in Fig. 18(a). The electric-field edge illumination of the simulation model shown in Fig. 4 at 26 GHz is plotted in Fig. 18(b), where an around -7 dB illumination taper can be observed. For the offset illumination case, a better aperture efficiency is usually obtained when the feeding beam is directed to a point deviation from the aperture center as explained in [28].

REFERENCES

[1] E. Basar, M. Di Renzo, J. De Rosny, M. Debbah, M. Alouini, and R. Zhang, "Wireless communications through reconfigurable intelligent surfaces," *IEEE Access*, vol. 7, pp. 116753–116773, 2019.

[2] C. Huang, A. Zappone, G. C. Alexandropoulos, M. Debbah, and C. Yuen, "Reconfigurable intelligent surfaces for energy efficiency in wireless communication," *IEEE Trans. Wireless Commun.*, vol. 18, no. 8, pp. 4157–4170, Aug. 2019.

[3] E. Basar and I. Yildirim, "Reconfigurable intelligent surfaces for future wireless networks: A channel modeling perspective," *IEEE Wireless Commun.*, vol. 28, no. 3, pp. 108–114, Jun. 2021, doi: 10.1109/MWC.001.2000338.

[4] I. Yildirim, A. Uyrus, and E. Basar, "Modeling and analysis of reconfigurable intelligent surfaces for indoor and outdoor applications in future wireless networks," *IEEE Trans. Commun.*, vol. 69, no. 2, pp. 1290–1301, Feb. 2021.

[5] L. Dai *et al.*, "Reconfigurable intelligent surface-based wireless communications: Antenna design, prototyping, and experimental results," *IEEE Access*, vol. 8, pp. 45913–45923, 2020.

[6] H. Yang *et al.*, "A 1-bit 10×10 reconfigurable reflectarray antenna: Design, optimization, and experiment," *IEEE Trans. Antennas Propag.*, vol. 64, no. 6, pp. 2246–2254, Jun. 2016.

[7] H. Kamoda, T. Iwasaki, J. Tsumochi, T. Kuki, and O. Hashimoto, "60-GHz electronically reconfigurable large reflectarray using single-bit phase shifters," *IEEE Trans. Antennas Propag.*, vol. 59, no. 7, pp. 2524–2531, Jul. 2011.

[8] E. Carrasco, M. Barba, and J. A. Encinar, "X-band reflectarray antenna with switching-beam using PIN diodes and gathered elements," *IEEE Trans. Antennas Propag.*, vol. 60, no. 12, pp. 5700–5708, Dec. 2012.

[9] P. Mei, S. Zhang, and G. F. Pedersen, "A low-cost, high-efficiency and full-metal reflectarray antenna with mechanically 2-D beam-steerable capabilities for 5G applications," *IEEE Trans. Antennas Propag.*, vol. 68, no. 10, pp. 6997–7006, Oct. 2020.

[10] S. Kisseleff, W. A. Martins, H. Al-Hraishawi, S. Chatzinotas, and B. Ottersten, "Reconfigurable intelligent surfaces for smart cities: Research challenges and opportunities," *IEEE Open J. Commun. Soc.*, vol. 1, pp. 1781–1797, 2020.

[11] M. A. El Mossallamy, H. Zhang, L. Song, K. G. Seddik, Z. Han, and G. Y. Li, "Reconfigurable intelligent surfaces for wireless communications: Principles, challenges, and opportunities," *IEEE Trans. Cogn. Commun. Netw.*, vol. 6, no. 3, pp. 990–1002, Sep. 2020.

[12] M. Di Renzo *et al.*, "Smart radio environments empowered by reconfigurable intelligent surfaces: How it works, state of research, and the road ahead," *IEEE J. Sel. Areas Commun.*, vol. 38, no. 11, pp. 2450–2525, Nov. 2020.

[13] A. Almohamad *et al.*, "Smart and secure wireless communications via reflecting intelligent surfaces: A short survey," *IEEE Open J. Commun. Soc.*, vol. 1, pp. 1442–1456, 2020.

[14] E. Björnson, Ö. Özdogan, and E. G. Larsson, "Reconfigurable intelligent surfaces: Three myths and two critical questions," *IEEE Commun. Mag.*, vol. 58, no. 12, pp. 90–96, Dec. 2020.

[15] M. Di Renzo *et al.*, "Reconfigurable intelligent surfaces vs. relaying: Differences, similarities, and performance comparison," *IEEE Open J. Commun. Soc.*, vol. 1, pp. 798–807, 2020.

[16] X. Tan, Z. Sun, J. M. Jornet, and D. Pados, "Increasing indoor spectrum sharing capacity using smart reflect-array," in *Proc. IEEE ICC*, May 2016, pp. 1–6.

[17] X. Tan, Z. Sun, D. Koutsonikolas, and J. M. Jornet, "Enabling indoor mobile millimeter-wave networks based on smart reflect-arrays," in *Proc. IEEE Conf. Comput. Commun.*, Apr. 2018, pp. 1–9.

[18] E. Bjornson and L. Sanguinetti, "Power scaling laws and near-field behaviors of massive MIMO and intelligent reflecting surfaces," *IEEE Open J. Commun. Soc.*, vol. 1, pp. 1306–1324, 2020.

[19] C. A. Balanis, *Antenna Theory: Analysis and Design*, 4th ed. Hoboken, NJ, USA: Wiley, 2016.

[20] A. Buffi, P. Nepa, and G. Manara, "Design criteria for near-field-focused planar arrays," *IEEE Antennas Propag. Mag.*, vol. 54, no. 1, pp. 40–50, Feb. 2012.

[21] R. C. Hansen, "Focal region characteristics of focused array antennas," *IEEE Trans. Antennas Propag.*, vol. AP-33, no. 12, pp. 1328–1337, Dec. 1985.

[22] S. Bildik, S. Dieter, C. Fritzsch, W. Menzel, and R. Jakoby, "Reconfigurable folded reflectarray antenna based upon liquid crystal technology," *IEEE Trans. Antennas Propag.*, vol. 63, no. 1, pp. 122–132, Jan. 2015.

[23] G. Perez-Palomino *et al.*, "Design and demonstration of an electronically scanned reflectarray antenna at 100 GHz using multiresonant cells based on liquid crystals," *IEEE Trans. Antennas Propag.*, vol. 63, no. 8, pp. 3722–3727, Aug. 2015.

[24] G. Perez-Palomino *et al.*, "Design and experimental validation of liquid crystal-based reconfigurable reflectarray elements with improved bandwidth in F-band," *IEEE Trans. Antennas Propag.*, vol. 61, no. 4, pp. 1704–1713, Apr. 2013.

[25] H. Yang *et al.*, "A study of phase quantization effects for reconfigurable reflectarray antennas," *IEEE Antennas Wireless Propag. Lett.*, vol. 16, pp. 302–305, 2016.

[26] M. R. Chaharmir, J. Shaker, M. Cuhaci, and A. Ittipiboon, "A broadband reflectarray antenna with double square rings," *Microw. Opt. Technol Lett.*, vol. 48, no. 7, pp. 1317–1320, Jul. 2006.

[27] *Rogers RO4350B Laminates*. Accessed: Dec. 2021. [Online]. Available: https://www.rogerscorp.com/-/media/project/rogerscorp/documents/advanced-electronics-solutions/english/data-sheets/ro4000-laminates-ro4003c-and-ro4350b—data-sheet.pdf

[28] A. Yu, F. Yang, A. Z. Elsherbeni, J. Huang, and Y. Rahmat-Samii, "Aperture efficiency analysis of reflectarray antennas," *Microw. Opt. Technol. Lett.*, vol. 52, no. 2, pp. 364–372, Feb. 2010.

Peng Mei (Member, IEEE) received the B.Eng. and M.Eng. (Hons.) degrees in electromagnetic field and microwave technology from the University of Electronic Science and Technology of China (UESTC), Chengdu, China, in 2015 and 2018, respectively, and the Ph.D. degree in electromagnetic field and microwave technology from Aalborg University, Aalborg, Denmark, in 2021.

He is currently working as a Post-Doctoral Researcher with the Antennas, Propagation, and Millimeter-Wave Systems (APMS) Section, Department of Electronic Systems, Aalborg University. His current research interests include periodic structures, metasurfaces, and millimeter-wave beam-steerable reflectarray/transmitarray antennas.

Dr. Mei was a recipient of the Outstanding Student of UESTC (only ten awardees every year of UESTC) in 2017, the Excellent Graduate Student of Sichuan Province in 2018, and the Excellent Master Thesis from the Chinese Institute of Electronics (CIE) in 2019. He served as the Section Chair of the IEEE-APS Topical Conference on Antennas and Propagation in Wireless Communications (APWC), Granada, Spain, in September 2019.

Yang Cai was born in Chengdu, Sichuan, China, in 1995. He received the B.Eng. and M.Eng. degrees in electromagnetic field and microwave technology from the University of Electronic Science and Technology of China (UESTC), Chengdu, China, in 2018 and 2021, respectively. He is currently pursuing the Ph.D. degree with the Antennas, Propagation, and Millimeter-Wave Systems (APMS) Section, Department of Electronic Systems, Aalborg University, Aalborg, Denmark.

His current research interests include periodic structures, metamaterial absorbers, and reconfigurable intelligent surfaces.

Kun Zhao received the B.S. degree in communication engineering from the Beijing University of Posts and Telecommunications (BUPT), Beijing, China, in 2010, and the M.S. and Ph.D. degrees from the KTH Royal Institute of Technology, Stockholm, Sweden, in 2012 and 2017, respectively.

He is currently an Industrial Post-Doctoral Researcher with the Antennas, Propagation, and Millimeter-Wave Systems (APMS) Section, Aalborg University, Aalborg, Denmark. He has been a Visiting Researcher with the Department of Electrical and Information Technology, Lund University, Lund, Sweden. His current research interests include mm-wave antenna and propagation, MIMO antenna systems, user body interactions, and body-centric wireless communications.

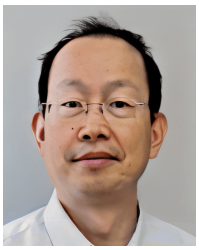

Zhinong Ying (Fellow, IEEE) received the M.S. (EE) degree from the Beijing University of Posts and Telecommunications (BUPT), Beijing, China, in 1986, and the Licentiate degree in engineering from the Chalmers University of Technology, Gothenburg, Sweden, in 1995.

In 1995, he joined Ericsson AB, Stockholm, Sweden, where he became a Senior Specialist in 1997 and an Expert in 2003 in his engineering career. He was also appointed as a Distinguished Engineer within the Sony Group globally. He has also been a part-time Professor with the Department of Electronic Systems, Aalborg University, Aalborg, Denmark, since 2021. He has authored and coauthored over 160 papers in various journals, conferences, and industry publications. He holds more than 170 patents pending in the antennas and new generation wireless network areas. He contributed to several book chapters on mobile antenna, small antenna, and MIMO antennas in "*Mobile Antenna Systems Handbook*" (3rd Edition) edited by H. Fujimoto and "*Handbook of Antenna Technologies*" edited by Z. N. Chen. He had contributed to a lot of work in innovative antenna designs and evaluation methods for the mobile industry. His main research interests include small antennas, broad and multiband antenna, multi-channel antenna (MIMO) systems, EM exposure research, and antenna and propagation in new generation mobile network, including massive MIMO, intelligent surface for smart radio environment, mm-wave and THz for mobile, and measurement techniques.

Dr. Ying became a fellow of the IEEE for his contribution to mobile terminal antenna technology. He received the Best Invention Award at Ericsson Mobile in 1996 and the Key Performer Award at Sony Ericsson in 2002. He was nominated for the President Award at Sony Ericsson in 2004 for his innovative contributions. He was a member of the Scientific Board of the ACE Program (Antenna Center of Excellent in European 6th frame) from 2004 to 2007.

Gert Frølund Pedersen (Member, IEEE) was born in 1965. He received the B.Sc. and E.E. (Hons.) degrees in electrical engineering from the College of Technology, Dublin Institute of Technology, Dublin, Ireland, in 1991, and the M.Sc.E.E. and Ph.D. degrees from Aalborg University, Aalborg, Denmark, in 1993 and 2003, respectively.

Since 1993, he has been with Aalborg University, where he is currently a Full Professor heading the Antennas, Propagation and Millimeter-Wave Systems Laboratory with 25 researchers. He is also the Head of the Doctoral School on wireless communication with some 40 Ph.D. students enrolled. He has published more than 500 peer-reviewed papers, six books, 12 book chapters, and holds over 50 patents. His research interests include radio communication for mobile terminals especially small antennas, diversity systems, propagation, and biological effects. He has also worked as a consultant for developments of more than 100 antennas for mobile terminals, including the first internal antenna for mobile phones in 1994 with lowest SAR, first internal triple-band antenna in 1998 with low SAR and high TRP and TIS, and lately various multiantenna systems rated as the most efficient on the market. He has worked most of the time with joint university and industry projects and have received more than $21 M in direct research funding. He is currently the Project Leader of the RANGE Project with a total budget of over $8 M investigating high performance centimeter/millimeter-wave antennas for 5G mobile phones. He has been one of the pioneers in establishing over-the-air measurement systems. The measurement technique is now well established for mobile terminals with single antennas and he was chairing the various COST groups with liaison to 3GPP and CTIA for over-the-air test of MIMO terminals.

Xian Qi Lin (Senior Member, IEEE) was born in Zhejiang, China, in July 1980. He received the B.Sc. degree in electronic engineering from the University of Electronic Science and Technology of China (UESTC), Chengdu, China, in 2003, and the Ph.D. degree in electromagnetic field and microwave technology from Southeast University, Nanjing, China, in 2008.

He joined the Department of Microwave Engineering, UESTC, in August, and became an Associate Professor and a Doctoral Supervisor in July 2009 and December 2011, respectively. From September 2011 to September 2012, he was a Post-Doctoral Researcher with the Department of Electromagnetic Engineering, KTH Royal Institute of Technology, Stockholm, Sweden. He is currently a Full Professor at UESTC. He has authored more than ten patents, more than 40 scientific journal articles, and has presented more than 20 conference papers. His research interests include microwave/millimeter-wave circuits, metamaterials, wireless power transfer, energy harvesting, and antennas.

Shuai Zhang (Senior Member, IEEE) received the B.E. degree from the University of Electronic Science and Technology of China (UESTC), Chengdu, China, in 2007, and the Ph.D. degree in electromagnetic engineering from the KTH Royal Institute of Technology, Stockholm, Sweden, in 2013.

He was a Research Fellow with KTH. In 2014, he joined Aalborg University, Aalborg, Denmark, where he currently works as an Associate Professor and the Leader of Antennas Group. In 2010, he joined Lund University, Lund, Sweden, as a Visiting Researcher. In 2011, he joined Sony Mobile Communications AB, Lund, as a Visiting Researcher. He was also an External Antenna Specialist at Bang & Olufsen, Struer, Denmark, from 2016 to 2017. He has coauthored over 100 articles in well-reputed international journals. He holds more than 16 (U.S. or WO) patents. His current research interests include mmWave antennas for cellular communications, biological effects, metasurfaces, CubeSat antennas, massive MIMO antennas, wireless sensors, and RFID antennas.